JGR Solid Earth

RESEARCH ARTICLE
10.1029/2022JB026174

Implications for Shallow Magma Transfer During the 2017 and 2018 Eruptions at Fernandina (Galápagos) Inferred From InSAR Data

Federico Galetto[1], Diego Reale[2], Eugenio Sansosti[2], and Valerio Acocella[3]

[1]Department of Earth and Atmospheric Sciences, Cornell University, Ithaca, NY, USA, [2]Istituto per il Rilevamento Elettromagnetico dell'Ambiente (IREA), National Research Council (CNR) of Italy, Naples, Italy, [3]Dipartimento di Scienze, Università degli Studi di Roma Tre, Rome, Italy

Abstract Previous work at Fernandina, the most active volcano of the Western Galápagos (Ecuador), revealed evidence for both a shallow and a deep magma reservoir, but the relative contribution of the two reservoirs to eruptions remains unclear. Here we investigate the September 2017 circumferential eruption and the June 2018 radial eruption using interferometric synthetic aperture radar data and geodetic modeling. Our results show that during the 2017 eruption magma was simultaneously withdrawn from the deep reservoir, injected upwards through the shallow reservoir, and then fed the circumferential feeder dike to the SW of the caldera. Two episodes of inflow of new magma occurred in both the deep and shallow magma reservoirs in the inter-eruptive period from December 2017 to May 2018. During the 2018 eruption, both reservoirs fed two radial feeder dikes below the north flank, probably interacting with an underlying peripheral melt pocket, and an inclined sheet below the NW sector of the caldera. Our results highlight the primary role of the deeper reservoir which accumulates most of the magma before eruptions. Both eruptions were characterized by rapid magma transfer from the deeper to the shallower reservoir. This is similar to what is observed at the nearby Wolf volcano, but unlike nearby Sierra Negra, where a shallower reservoir accumulates higher volumes of magma before eruptions. These differences in the pre-eruptive role of the deeper and shallower reservoirs might be related to the different evolutionary stages of Fernandina and Wolf with regard to the more mature Sierra Negra.

Plain Language Summary Fernandina is the most active volcano of the Western Galápagos (Ecuador). Two magma reservoirs at different depths below the volcano trigger eruptions both near the caldera rim (circumferential eruptions) and lower on the volcano flanks (radial eruptions). The role played by the two reservoirs in the eruptions is poorly understood. Here we studied the 2017 and the 2018 eruptions that occurred at Fernandina by using deformation data derived from radar satellites to investigate the inputs and outputs of new magma into the two reservoirs when eruptions occurred. The 2017 eruption had similar characteristics to the 2005 eruption, while the 2018 eruption had more complex mechanisms of shallow magma transfer, with magma transported in multiple directions below the north flank of Fernandina. We found that rapid magma transfer from the deep to the shallow reservoir provided most of the magma for both eruptions, similar to the nearby Wolf volcano, and unlike nearby Sierra Negra, a feature that may be due to the evolutionary stage of the volcanoes.

Key Points:

- The 2017 circumferential eruption at Fernandina shows similar characteristics to the 2005 eruption, occurred in the same area
- The 2018 eruption is connected to the propagation of multiple dikes and sills, with most of the magma remaining intruded
- Both eruptions were characterized by rapid magma transfer from the deeper to the shallower reservoir, similar to what is observed at Wolf

Supporting Information:

Supporting Information may be found in the online version of this article.

Correspondence to:

F. Galetto,
fg253@cornell.edu

Citation:

Galetto, F., Reale, D., Sansosti, E., & Acocella, V. (2023). Implications for shallow magma transfer during the 2017 and 2018 eruptions at Fernandina (Galápagos) inferred from InSAR data. *Journal of Geophysical Research: Solid Earth*, *128*, e2022JB026174. https://doi.org/10.1029/2022JB026174

Received 2 DEC 2022
Accepted 21 MAY 2023

Author Contributions:

Conceptualization: Federico Galetto, Eugenio Sansosti, Valerio Acocella
Data curation: Federico Galetto, Diego Reale, Eugenio Sansosti
Formal analysis: Federico Galetto, Diego Reale
Investigation: Federico Galetto, Diego Reale, Eugenio Sansosti
Methodology: Federico Galetto, Diego Reale, Eugenio Sansosti
Project Administration: Eugenio Sansosti
Resources: Eugenio Sansosti, Valerio Acocella
Supervision: Diego Reale, Eugenio Sansosti, Valerio Acocella
Validation: Federico Galetto, Eugenio Sansosti, Valerio Acocella

1. Introduction

Basaltic shields with summit calderas are among the most active volcanoes on Earth, experiencing repeated eruptions over decades (Bagnardi et al., 2013; Galetto et al., 2023; Peltier et al., 2018; Smets et al., 2015). These eruptions can be characterized by complex mechanisms of shallow magma transfer that can also change from one eruption to another (Bagnardi et al., 2013; Chadwick et al., 2011; Davis et al., 2021; Dumont et al., 2022; Shreve et al., 2021; Smittarello et al., 2022). Understanding the propagation paths of magma from a reservoir to the surface is important for forecasting how magma might be transferred in future eruptions (Bagnardi et al., 2013; Davis et al., 2021). The basaltic shields of the western Galápagos experience both circumferential eruptions near the caldera rims and radial eruptions lower on the volcano flanks (Bagnardi et al., 2013; Chadwick & Howard, 1991; Davis et al., 2021; Galetto et al., 2020; Geist et al., 2008). Circumferential eruptions at Galápagos volcanoes result from dikes fed from sub-horizontal sills that steepen as they intrude upward to become dikes

Visualization: Federico Galetto, Diego Reale, Valerio Acocella
Writing – original draft: Federico Galetto, Diego Reale, Eugenio Sansosti, Valerio Acocella

below the caldera margins (Bagnardi et al., 2013; Chadwick et al., 2011). Radial dikes are interpreted to form by the propagation of a sub-horizontal sill that twists around a radial horizontal axis during its propagation to the surface (Jónsson et al., 1999; Bagnardi et al., 2013; Galetto et al., 2020; Davis et al., 2021).

The western Galápagos volcanoes, with the possible exception of Cerro Azul, are characterized by a complex architecture within their magmatic systems, with at least two main magma reservoirs: a shallower one (~1–2 km below the surface) and a deeper one (with a top at ~5 km below the surface) (Geist et al., 2014; Stock et al., 2020). An important and unresolved question is what is the role of these two reservoirs in feeding the propagation of circumferential and radial eruptions. The relative contributions of the two reservoirs in feeding eruptions are crucial to understand the eruptive dynamics of Galápagos volcanoes and for forecasting purposes (Galetto et al., 2022; Gregg et al., 2022). In fact, the accumulation of magma in a deeper reservoir may not necessarily generate a detectable uplift signal at the surface (Stock et al., 2018); therefore pre-eruptive magma accumulation in the deep reservoir may pass unnoticed, making forecasting more difficult.

Here we have studied the September 2017 circumferential eruption and the June 2018 radial eruption that occurred at Fernandina (Galápagos) to better understand the roles of the shallower and deeper reservoirs and the mechanisms of shallow magma transfer. We used interferometric synthetic aperture radar interferometry (InSAR) to document the surface deformation associated with both eruptions. Then we invert the observed deformation for possible magmatic sources by using geodetic modeling. The results show that the September 2017 eruption was fed by dikes similar in geometry and location to Fernandina's 2005 eruption (Chadwick et al., 2011). In contrast, the June 2018 eruption differs from the 1995 and 2009 radial eruptions at Fernandina, and all other radial recent eruptions occurred elsewhere in the Galápagos (Jónsson et al., 1999; Bagnardi et al., 2013; Galetto et al., 2020; Davis et al., 2021). However, both eruptions seem characterized by sudden and rapid magma transfer from the deep reservoir to the shallow one, suggesting that the connectivity of the two reservoirs has a main role in driving most of the eruptions at Fernandina, similar to what is observed at the nearby Wolf volcano (Stock et al., 2018) and unlike what observed at Sierra Negra volcano (Bell et al., 2021; Chadwick et al., 2006; Geist et al., 2008; Vasconez et al., 2018).

2. Geological Background

The Galápagos Archipelago is a hot spot magmatic province in the eastern Pacific Ocean. The islands lie above a broad and thick platform over young (<10 Ma) oceanic lithosphere (Figure 1; Feighner & Richards, 1994). The current volcanic activity mainly focuses on the seven shield volcanoes forming the western Galápagos Islands of Fernandina and Isabela, in the upwelling region of the hot spot (Amelung et al., 2000; Gibson & Geist, 2010; Hooft et al., 2003; Poland, 2014; Stock et al., 2020; Villagómez et al., 2014). These volcanoes are large, flexurally supported shields with summit calderas, forming a distinct volcanological, petrological, geochemical, and structural group with respect to the eastern Galápagos volcanoes (Feighner & Richards, 1994; Harpp & Geist, 2018; White et al., 1993). Fernandina is the westernmost and most active volcano in the western Galápagos (Figure 1), with an elevation of 1476 m above sea level, gently sloping lower flanks, steep upper slopes and a 1100 m deep caldera (Bagnardi & Amelung, 2012; Munro & Rowland, 1996; Naumann & Geist, 2000). The 6.5 × 4.6 km wide caldera, with its major axis oriented NW-SE, results from repeated cycles of collapse and is the largest in volume (12.4 km^3) among those of the western Galápagos (Munro & Rowland, 1996; Naumann & Geist, 2000). The last caldera collapse (about 1–2 km^3; Simkin & Howard, 1970; Howard et al., 2019) occurred in 1968.

Previous studies have provided evidence that Fernandina has at least two connected magma reservoirs, at about 1 and 5 km below sea level (b.s.l.) (Bagnardi & Amelung, 2012; Chadwick et al., 2011). Inter-eruptive uplift of the caldera area revealed by geodetic monitoring (InSAR + GPS) is thought to result from the inflow of new magma into the shallow reservoir, while deformation of the edifice outside the caldera is usually associated with the deeper reservoir (Bagnardi & Amelung, 2012; Chadwick et al., 2011). At least 17 eruptions have occurred at Fernandina since 1961 (Global Volcanism Program, 2013) through a distinctive pattern of circumferential fissures just outside the caldera rim and radial fissures lower on the volcano's flanks (Bagnardi et al., 2013; Chadwick & Howard, 1991). The stress field allowing the formation of both types of eruptive fissure is mainly controlled by the unloading due to caldera collapse, the load of the volcanic edifice, the stresses added from previous intrusions and the pressurization of the magma reservoir (Bagnardi et al., 2013; Chadwick & Dieterich, 1995; Chestler & Grosfils, 2013; Corbi et al., 2015, 2016; Gaete et al., 2019). The local stress conditions within the

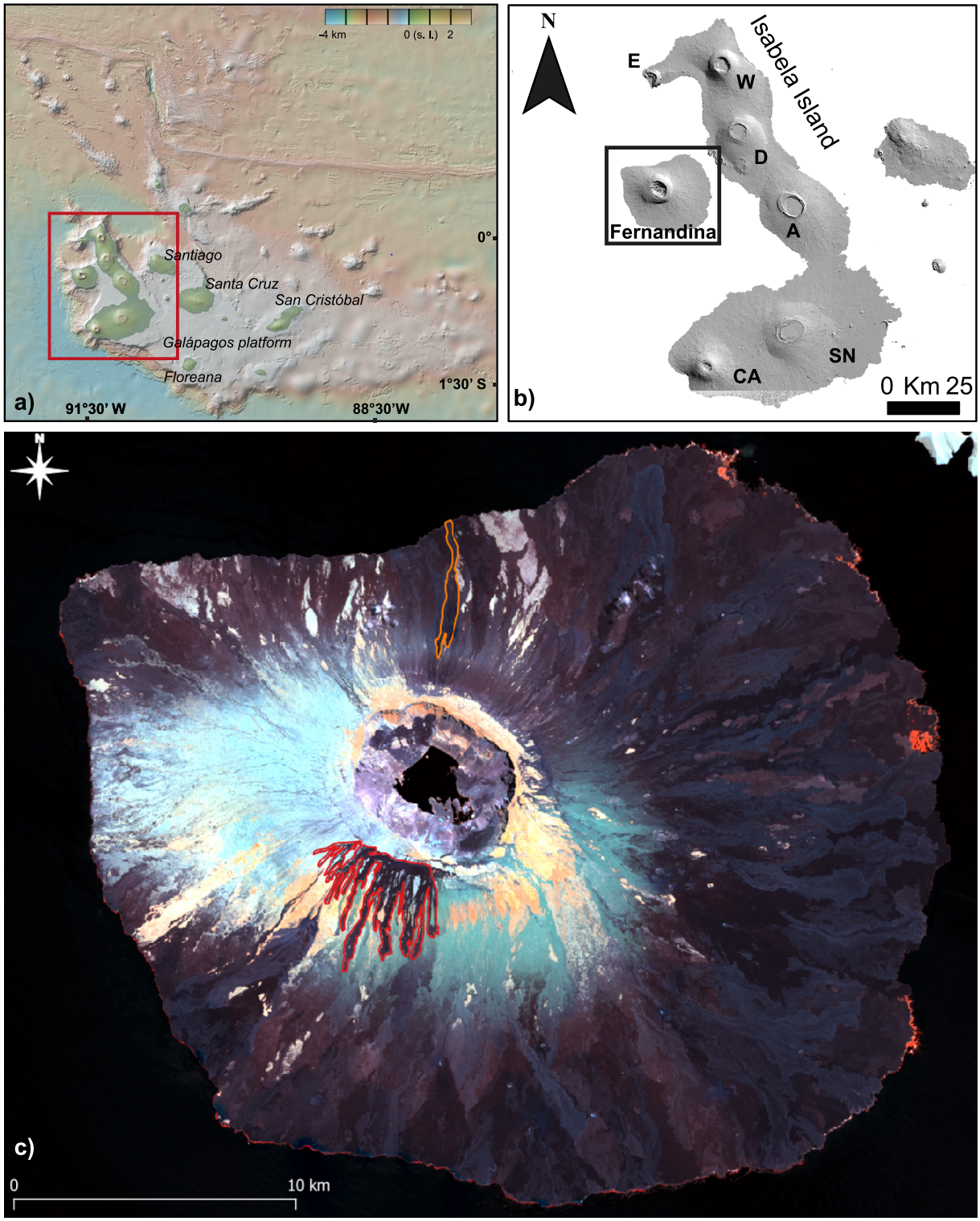

Figure 1. (a) Galápagos Archipelago. The red square outlines the extent of Panel (b). Digital elevation model and bathymetry from GeoMappApp. (b) The western Galápagos Islands of Fernandina (the black square is the area in Panel (c) and Isabela. (c) Landsat 8 image of Fernandina acquired on 17 August 2019 (false colors image R = Band 5; G = Band 6; B = Band 7). We outlined in red the lava flows erupted in September 2017 and in orange lava flow erupted in June 2018.

volcano slopes, the topography of the volcanic edifice and any pre-existing discontinuity control the dip of the radial intrusions (Corbi et al., 2015; Davis et al., 2021).

The 2017 eruption started on 4 September along a circumferential fissure near the southern caldera rim (Figure 1), in the same area of the 2005 circumferential eruption (Chadwick et al., 2011; Vasconez et al., 2018). The 2017 eruption produced $9.7 \pm 4.9 \times 10^6$ m^3 (DRE) of lava (Vasconez et al., 2018). In contrast, the 16 June 2018 eruption occurred along a radial fissure located on the northern flank (Figure 1), on the opposite side of the volcano from the last two radial eruptions of Fernandina in 1995 and 2009 that occurred on the SW flank (Jónsson et al., 1999; Bagnardi et al., 2013). The 2018 eruption generated $5.9 \pm 3 \times 10^6$ m^3 (DRE) of lava (Vasconez et al., 2018). Further details on the 2017 and 2018 eruptions at Fernandina are reported in Vasconez et al. (2018). Finally, the 2018 eruption was followed in January 2020 by a circumferential eruption near the eastern caldera rim (Bernard et al., 2022; Vasconez et al., 2022).

3. Methods

3.1. InSAR Data Processing

To measure surface deformation before, during and after the 2017–2018 eruptions at Fernandina, we used InSAR data. We processed 68 SAR images acquired by the Italian Space Agency's COSMO-SkyMed (CSK) satellites (X-band, wavelength $\lambda = 3.1$ cm) in HIMAGE (stripmap) mode. We used 34 images from an ascending track (acquisition beam H4-17, corresponding to an average look angle of about 51°) acquired between 12 August 2017 and 22 January 2019, and 34 from a descending track (acquisition beam H4-19, look angle of about 53°) acquired between 29 July 2017 and 8 January 2019; in both cases the acquisitions were regular, with a constant repeat interval of 16 days. Unfortunately, CSK data before July/August 2017 have a temporal gap of about 5 months in the acquisition sequence on both orbits, thus impairing the 2017 pre-eruptive analysis.

To further investigate the deformation patterns associated with the two eruptive events, we have also processed eight additional SAR images acquired in Interferometric Wide (IW) Swath mode by the Copernicus Sentinel-1 (S1) satellites (C-band, wavelength $\lambda = 5.63$ cm), just between the two considered eruptions (August–September 2017 and June–July 2018). We used four images (2017/08/22–2017/09/15 and 2018/05/25–2018/06/30 pairs) from an ascending track (path 106, look angle ∼41.5°) and four images (2017/08/23–2017/09/16 and 2018/05/26–2018/07/01 pairs) from a descending one (path 128, look angle ∼36.5°).

We first generated differential interferograms by means of the geometrical registration approach (Sansosti et al., 2006) and then removed the topographic contribution to the interferometric phase using the TanDEM-X 12 m Digital Elevation Model (DEM) from the German Aerospace Center (DLR) (Krieger et al., 2007). Furthermore, we performed the model-based phase unwrapping by using the approach in Fornaro et al. (2011) which combines the CSK data through a multi-temporal (MT) approach based on the Small BAseline Subset (SBAS) method (Berardino et al., 2002). Among others, one advantage of using a MT approach is the capability to estimate and filter the atmospheric contribution, thus allowing us to separate the deformation signals from atmospheric noise. This characteristic is particularly important when dealing with low amplitude deformation signals, such as in the case of pre- and post-eruptive periods for which the deformation signal is significantly smaller than that measured across the main eruptive events.

3.2. Geodetic Modeling

To constrain the sources of deformation, we inverted the Sentinel-1 and COSMO-SkyMed Line of Sight (LOS) displacement measurements. We estimated deformation source parameters and uncertainties using the Bayesian approach implemented in the Geodetic Bayesian Inversion Software (GBIS; Bagnardi & Hooper, 2018). The inversion algorithm uses a Markov-chain Monte Carlo method, incorporating the Metropolis-Hastings algorithm, to find the posterior Probability Density Functions (PDFs) of model parameters. For each observational interval, the corresponding ascending and descending LOS data were jointly inverted to better constrain the deformation source parameters.

Through the Bayesian approach we sampled the joint posterior PDF for the model parameters, taking into account uncertainties in the data, which were directly quantified using experimental semivariograms calculated from the data, and approximated by unbounded exponential one-dimensional functions with a nugget (Bagnardi & Hooper, 2018). To reduce the computational burden, InSAR data were subsampled using an adaptive quadtree method (Bagnardi & Hooper, 2018; Decriem et al., 2010). In each inversion, we sampled the posterior PDFs

through 1,000,000 iterations. The sources used for the inversion were: a point source (Mogi, 1958), a prolate ellipsoid (Yang et al., 1988) and a rectangular dislocation with uniform opening (Nikkhoo et al., 2017; Okada, 1985). For all the models we assumed an isotropic elastic half-space with Poisson's ratio $\nu = 0.25$.

Deformation connected to the deep magma reservoir of Fernandina was previously modeled by using both a Mogi source (Chadwick et al., 2011) and a horizontal Yang source (Bagnardi & Amelung, 2012; Bagnardi et al., 2013). Here we used a Mogi source in most of the cases, since it requires fewer parameters. However, we used a Yang source for the 2017 eruption and for the September 2018–January 2019 deformation, since this source provided a better-fit to the elongated deformation pattern associated with these two events. To reduce the number of variables, in all the inversions we fixed the depth of the two magma reservoirs at 1,080 and 5,000 m below the surface, consistent with previous results (Bagnardi et al., 2013; Chadwick et al., 2011).

The combination of sources used for modeling the shallow intrusions from the reservoirs during the different episodes of deformation has been obtained with a trial-and-error approach. We started by testing the combination of source used for modeling previous deformations at Fernandina (Bagnardi & Amelung, 2012; Bagnardi et al., 2013; Chadwick et al., 2011). When these did not provide satisfying solutions (unrealistic or with large residuals), we modified them to obtain a combination of sources and parameters that were realistic and significantly reduced the residuals.

4. InSAR Data

For a comprehensive analysis of the two eruptions, we separately analyze different time intervals, including pre-, syn-, and post-eruption events.

4.1. The 4–7 September 2017 Eruption

The September 2017 eruption occurred along a circumferential fissure outside the southern caldera rim, near the 2005 circumferential eruptive fissure. CSK and Sentinel-1 data show consistent deformation measurements after accounting for the different look angles. Moreover, the syn-eruptive deformation pattern recorded by InSAR data from both sensors and both ascending and descending orbits (Figures 2a–2d) is similar in position and geometry to that observed during the 2005 eruption (Chadwick et al., 2011). Ascending interferograms (Figures 2a and 2c for CSK and S1, respectively) show a positive (toward satellite) LOS deformation of 30–38 cm in the SW part of the caldera rim and a negative (away from satellite) LOS deformation in the southern part of the rim (Figure S1 in Supporting Information S1). This deformation pattern is almost reversed on descending interferograms (Figures 2b and 2d for CSK and S1, respectively; Figure S2 in Supporting Information S1) due to the predominance of horizontal (east-west) ground displacements (Figures S3a and S3b in Supporting Information S1). The caldera floor shows a negative LOS signal in both ascending and descending data, which is indicative of a prevalent subsidence (Figure S3a in Supporting Information S1).

4.2. Inter-Eruptive Period

From December 2017 to February 2018, we measure positive LOS displacements (toward the satellite) both within the caldera floor and along the upper flanks of Fernandina, with a maximum of about 8 cm in the ascending and about 10 cm in the descending CSK data, respectively (Figures 2e and 2f). The LOS deformation maximum is shifted to the west of the caldera center on ascending orbit data and to the east on descending ones (Figures 2e and 2f), which is indicative of inflation.

In the following three months (February-May 2018) there is a change in the deformation pattern, with the signal becoming more focused within the caldera floor, with a positive LOS deformation of 13–14 cm (Figures 2g and 2h). The deformation rate of the caldera floor is similar to that of the previous months, increasing slightly from 0.1 to 0.13 cm/day (December–February) to 0.14–0.15 cm/day. LOS displacement outside the caldera is still present, although over a smaller area, with opposite signs on the eastern and western sides of edifice. In particular, on ascending orbit data (Figure 2g), this signal is positive on the western side of the volcano and negative on the eastern side, while the configuration is reversed for descending orbit data (Figure 2h).

4.3. The 16–21 June 2018 Eruption

The June 2018 eruption occurred along a radial eruptive fissure on the north flank of the volcano. Again, a large deformation signal on the north flank is measured consistently on both CSK (Figures 2i and 2j) and Sentinel-1

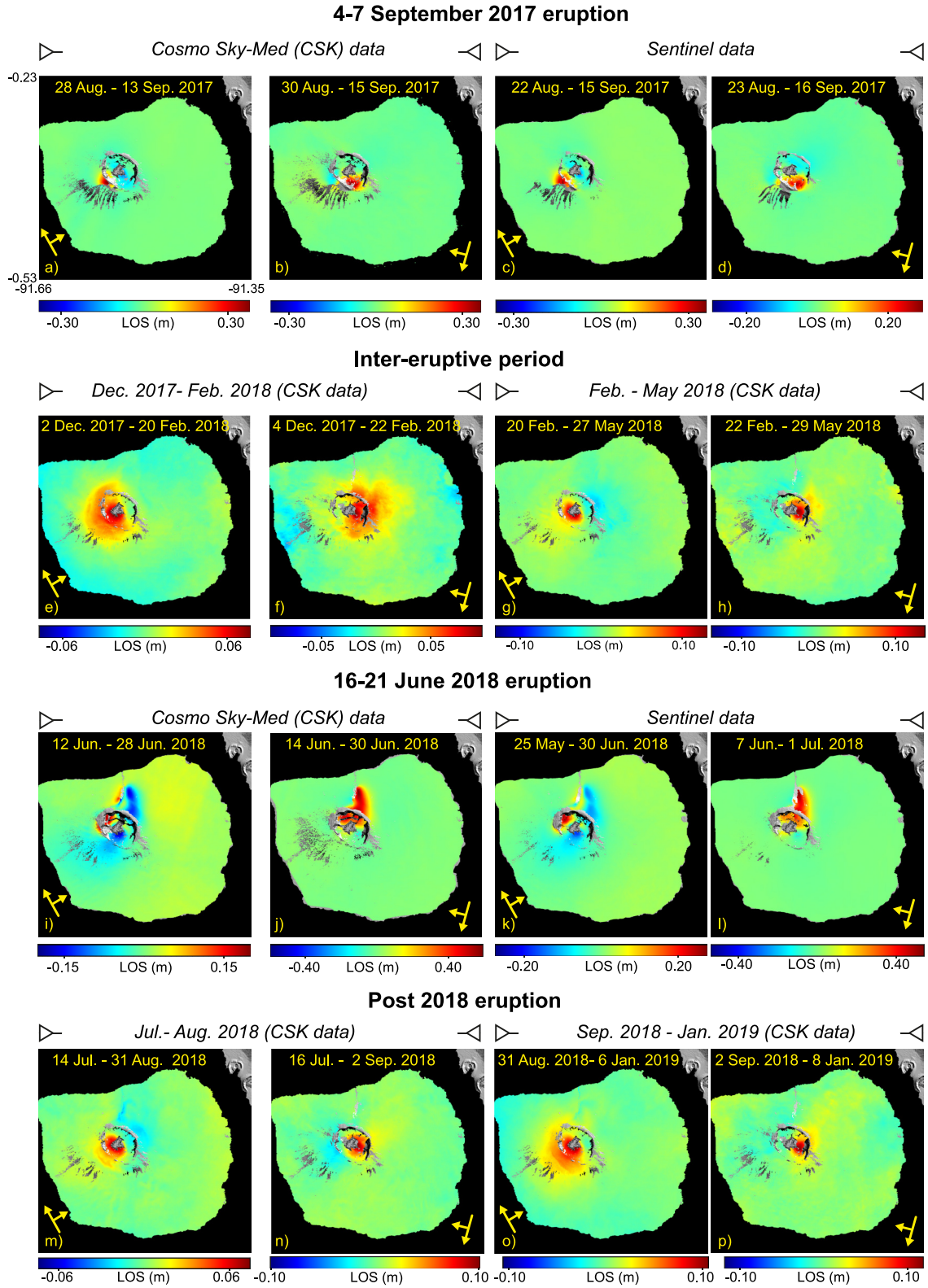

Figure 2. InSAR LOS displacements of Fernandina from September 2017 to January 2019 (positive values toward satellite). (a–d) LOS displacement of the September 2017 eruption from COSMO-SkyMed (a and b) and Sentinel-1 (c and d) data. (e and f) LOS displacement from December 2017 to February 2018 (COSMO-SkyMed data). (g and h) LOS displacement from February to May 2018 (COSMO-SkyMed data). (i–l) LOS displacement during the June 2018 eruption (COSMO-SkyMed) (i and j) and Sentinel-1 (k and l) data. LOS displacements from July to August 2018 (m and n) and from September 2018 to January 2019 (o and p) from COSMO-SkyMed data.

(Figures 2k–2l) data. This signal reaches a positive LOS displacement of about 53–59 cm (toward the satellite) on the descending tracks, and a negative LOS displacement of about 15 cm (away from the satellite) on the ascending tracks (Figures S1 and S2 in Supporting Information S1). This is due to a significant eastward component of displacement associated with a clear and strong uplift (Figures S3c and S3d in Supporting Information S1). To the west of this area, a signal with opposite characteristics (i.e., positive LOS displacement on ascending data and negative on descending) is detected, although with smaller amplitude. Such a signal is consistent with a westward component of the displacement in this area (Figure S3d in Supporting Information S1). Therefore, the two portions of the flank across the eruptive fissure moved in opposite directions, the western part moving westward, the eastern part moving eastward, although with different displacement magnitudes (Figure S3d in Supporting Information S1).

Inside the caldera, the ascending data show a negative LOS displacement of 11–20 cm mainly in the south part and a positive LOS displacement (>20–30 cm) in the NW sector. Such a positive displacement is present also on descending tracks, although located more toward the north.

4.4. Post June 2018

The deformation pattern observed from July to August 2018 (Figures 2m–2n) is quite similar to that of the February-May 2018 time interval (Figures 2g and 2h) in both shape and amplitude. Indeed, it is mainly focused within the caldera, with a positive LOS deformation of 7–10 cm on both ascending and descending tracks. A LOS deformation of 3–4 cm, with opposite sign in the NE and SW flanks on the ascending and descending tracks respectively, is detected immediately outside the caldera rim. The deformation rate (0.15–0.2 cm/day) is slightly higher than that observed from February to May.

In the final period of our analysis, from September 2018 to January 2019, positive LOS deformation is maximum within the caldera, where it reaches about 11–12 cm (Figures 2o–2p). Thus, the associated deformation rate (0.09 cm/day) is lower than that observed in the previous months. We also note a deformation signal outside the caldera in the SW and NE portions of the upper flanks for the ascending and descending orbits, respectively. Deformation signals are now dominated by positive displacements and, especially on the ascending tracks, involve large portions of the upper SW flank (Figure 2o).

5. Geodetic Modeling Results

5.1. 4–7 September 2017 Eruption

We model the Sentinel-1 data associated with the September 2017 eruption using three inflating Rectangular dislocation (RD) sources representing intruded dikes, a deflating horizontal RD source and a deflating ellipsoid (Figure 3) that represent the shallow and deep reservoirs, respectively (Bagnardi et al., 2013). To reduce the number of variables, we fix some model parameters (see Table S1 for details) based on the location of the eruptive fissures, consistent with the solutions obtained by Chadwick et al. (2011) for the 2005 circumferential eruption at Fernandina, associated with a similar set of eruptive fissures and a similar deformation pattern and on the solutions obtained by Bagnardi et al. (2013). The circumferential dike is modeled by using two RD sources: a slightly inclined sill (26°), connected to the lower portion of the shallow reservoir, with a volume change of $3.97 \pm 0.17 \times 10^6$ m^3 and an inclined dike (71°) whose upper edge is coincident with the eruptive fissures, with a volume change of $0.66 \pm 0.24 \times 10^6$ m^6 (Figure 3 and Table S1). The shallow magma reservoir of Fernandina was modeled as a horizontal RD source with volume loss of $-0.46 \pm 0.03 \times 10^6$ m^6. Similar to Bagnardi and Amelung (2012), we model the deeper magma reservoir by using a horizontal ellipsoid with volume loss of $-9.71 \pm 1.38 \times 10^6$ m^3, obtained using the equation in Tiampo et al. (2000) (Table S1). Finally, the last RD source is a vertical dike placed in between the two magma reservoirs, with a positive volume change of $5.01 \pm 0.52 \times 10^6$ m^3 (Table S1).

We test the same combination of sources also on COSMO-SkyMed data, finding similar results (Table S2; Figures S4 and S5 in Supporting Information S1).

5.2. December 2017–February 2018 (Inter-Eruptive Period)

We model the deformation from December 2017 to February 2018 using a combination of a deeper Mogi source and a shallower horizontal rectangular dislocation (sill-like) source (Figure 4; Table S3), similar to Chadwick

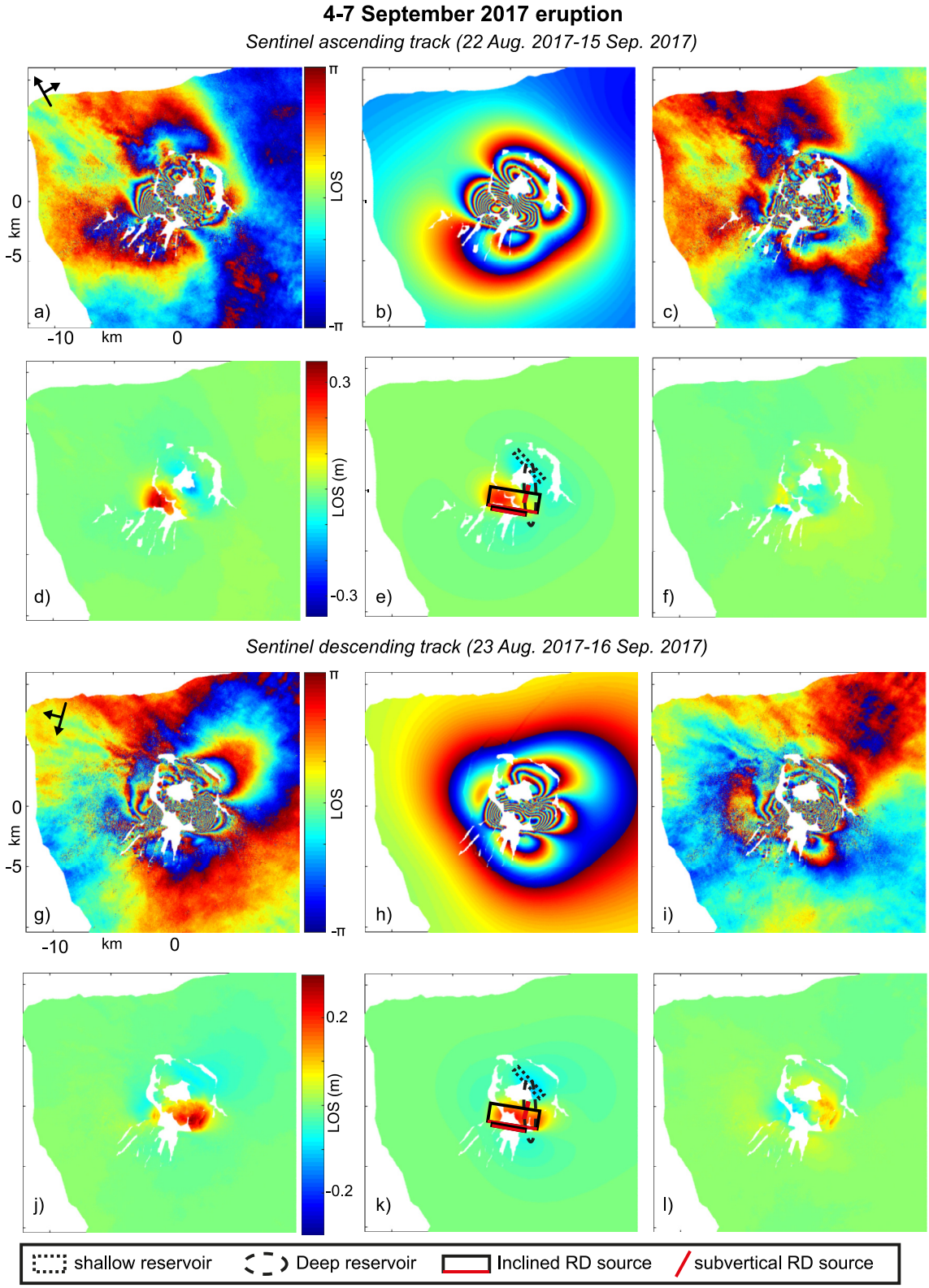

Figure 3. Wrapped (a and g) and unwrapped (d and j) Sentinel-1 LOS displacements for the September 2017 eruption. (b, e, h, and k). Predicted displacements (four RD models and one Yang model) using the maximum a posteriori probability solutions (MAP). (c, f, i, and l). Related residuals. (a–c and g–i) Each fringe (full color cycle) represents 2π radians of phase change corresponding to 2.8 cm of range change in the LOS direction. (e and k) The rectangles on model plots represent the outline of the optimal RD planes with the red thicker line outlining their updip edge (no red line if the RD is horizontal). The dotted ellipse represents the outline of the optimal Yang source. The origin (bottom left) for all panels is: −91.55° and −0.3795°.

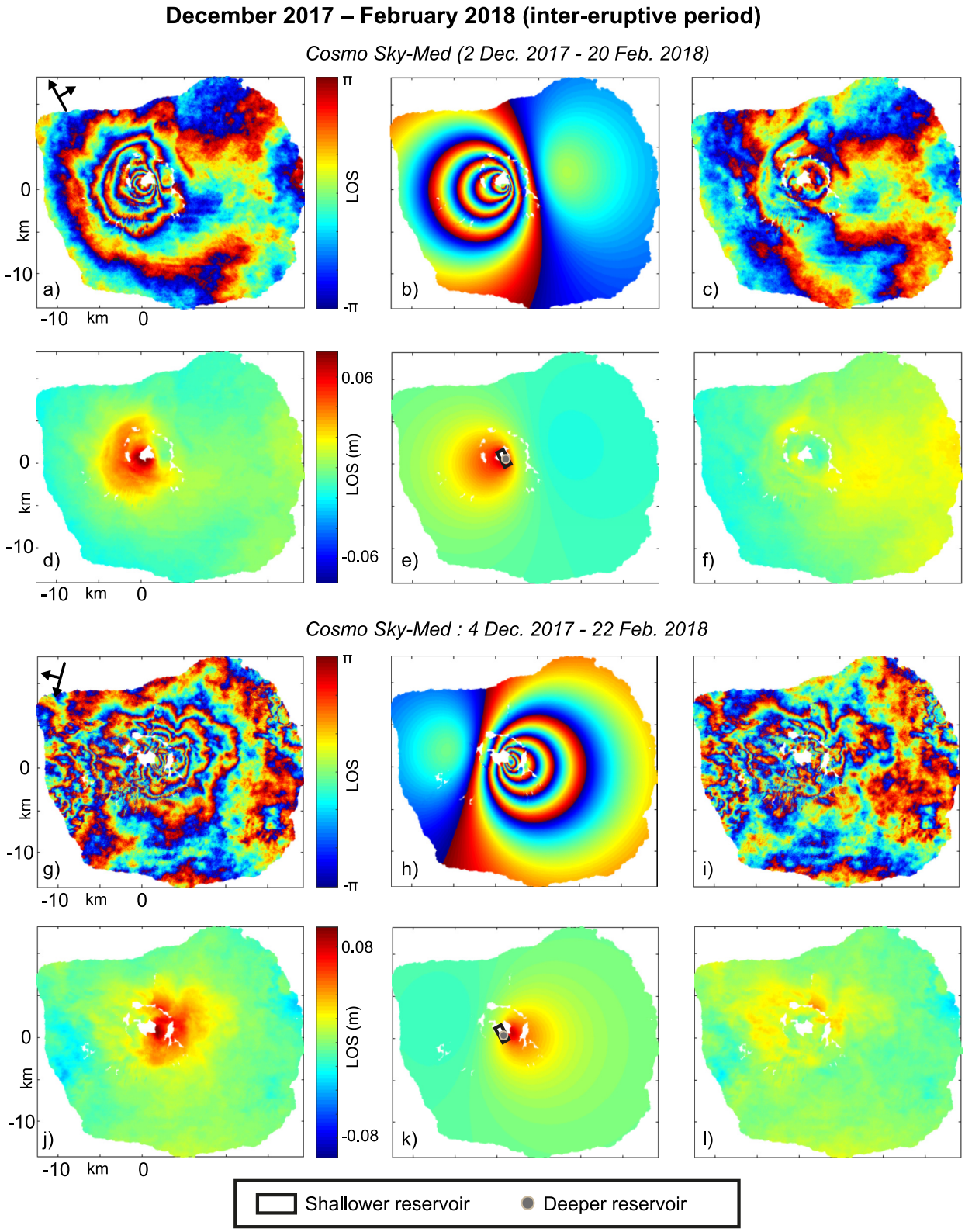

Figure 4. Wrapped (a and g) and unwrapped (d and j) COSMO-SkyMed LOS displacements for the December 2017–February 2018 period (inter-eruptive period). (b, e, h, and k) Predicted displacements (one RD model and one Mogi model) using the MAP solutions. (c, f, i, and l) Related residuals. (a–c and g–i) Each fringe (full color cycle) represents 2π radians of phase change corresponding to 1.55 cm of range change in the LOS direction. (e and k) The black rectangle is the position and geometry of the horizontal RD model, while the gray dot is the position of the Mogi source. The origin for all panels is: −91.55° and −0.3795°.

et al. (2011) for modeling similar deformation patterns at Fernandina (Figure 4). The Mogi source converges to a volume change of $7.48 \pm 0.78 \times 10^6$ m^3, while the RD source converges to a 1.9×0.8 km sill with a volume change of $0.265 \pm 0.035 \times 10^6$ m^3 (Table S3).

5.3. February 2018–May 2018 (Inter-Eruptive Period)

To model the deformation pattern observed between February and May 2018, we use a Mogi and a horizontal RD source for the deeper and shallower magma reservoirs of Fernandina, respectively (Bagnardi & Amelung, 2012; Chadwick et al., 2011), plus an inclined RD source (dike-like source) (Figure 5). The latter was introduced to remove the low-intensity deformation signal on the east flank, immediately outside the caldera rim. We fix the dip angle of the inclined RD (60°; dike-like; Table S4), since the low signal-to-noise ratio and the low magnitude of the associated displacements do not promote a good convergence of this parameter. The fixed dip angle is estimated based on the observed deformation pattern (see Section 4.2), typical of an inclined dike (Lisowski, 2007). The Mogi source converges for a positive volume change of $3.12 \pm 0.73 \times 10^6$ m^3, while the horizontal RD source (sill-like) converges to a 3×1.55 km horizontal sill with volume change of $1.06 \pm 0.06 \times 10^6$ m^3 (Table S4). Finally, for the inclined dike, the Bayesian analysis converges to a 2.9×1.7 km dike, whose top edge is placed at about 0.97 ± 0.16 km below the caldera floor, with volume change of $1.10 \pm 0.23 \times 10^6$ m^3 (Table S4).

5.4. 16–21 June 2018 Eruption

Radial fissure eruptions at Fernandina generate complex deformation patterns that often require the combination of many model sources to approximate complex magma pathways (e.g., Bagnardi et al., 2013). In this case, the best solution for the inversion of Sentinel-1 data reproducing the observed deformation pattern is obtained, after a trial-and-error approach where we tested different sources combinations, by using five inclined and connected RD sources, one horizontal RD source, one Mogi source, and one Yang source (Figure 6). Still, with all these sources the model did not result in optimal convergence of all the parameters, for example, generating unrealistic solutions like feeder dikes not coinciding with the location of the eruptive fissures. To overcome these problems, we fix some of the source parameters (see Table S5 for details) to values that could be justified geologically and/or by the previous modeling results obtained for similar radial dikes at Fernandina, as previously done by Chadwick et al. (2011) and Bagnardi et al. (2013) for the 2005 and 2009 eruptions. As for the sources used for modeling the two reservoirs (the Mogi and the horizontal RD), results of the Bayesian analysis converge to a Mogi source which lost $-13.15 \pm 0.5 \times 10^6$ m^3 of magma and to a 1.2×0.7 km RD source which lost $-0.618 \pm 0.013 \times 10^6$ m^3 of magma (Table S5). We model the deformation in the NW sector of the caldera using a RD source. We fix the depth and the dip angle of this RD source similar to the solution obtained by Bagnardi et al. (2013) for the initial propagating sill successively forming a radial dike during the 2009 radial eruption. The Bayesian analysis converges to a volume change of $6.012 \pm 0.084 \times 10^6$ m^3 (Table S5). The complex deformation pattern observed in the north sector of the caldera and on the northern flank is modeled using 4 RD pressurized sources and a horizontal deflating Yang source. The volume changes of the four RD sources, from S to N, are respectively of $0.297 \pm 0.016 \times 10^6$, $3.495 \pm 0.131 \times 10^6$, $1 \pm 0.07 \times 10^6$, and $1.492 \pm 0.046 \times 10^6$ m^3 (see Table S5 for details). In contrast, the Yang source shows a volume loss of $-1.417 \pm 0.115 \times 10^6$ m^3, obtained using the procedure in Tiampo et al. (2000) (Table S5).

The residual fringes in the area of the radial dikes are likely related to further complexities in the geometry of the dikes, to inelastic deformation associated with fracturing and to the necessity to subsample data before the inversion (Decriem et al., 2010). Further complexities in the geometries of the sources and subsampling could also explain the residuals within the caldera.

We use the same sources to model the CSK data (Figures S6 and S7 in Supporting Information S1 and Table S6). Despite the overall consistency in the solutions with the Sentinel-1 data, some differences in terms of volume change remain. The main differences are the volume change of the Mogi and the Yang sources, with the results of the Bayesian analysis that converge to a Mogi source which lost $-9.09 \pm 0.41 \times 10^6$ m^3 of magma and to a Yang source losing $-1.84 \pm 0.3 \times 10^6$ m^3. The other sources show volume changes similar to that obtained from the inversion of Sentinel-1, with the shallow magma reservoir losing $-0.77 \pm 0.03 \times 10^6$ m^3 of magma, while the volume changes of the four RD sources, from S to N, are respectively of $0.44 \pm 0.02 \times 10^6$, $2.37 \pm 0.23 \times 10^6$, $2.14 \pm 0.04 \times 10^6$ and $1.4 \pm 0.03 \times 10^6$ m^3 (Table S6). The intruded sill in the NW sector of the caldera has a volume change of $5.79 \pm 0.07 \times 10^6$ m^3 (Table S6).

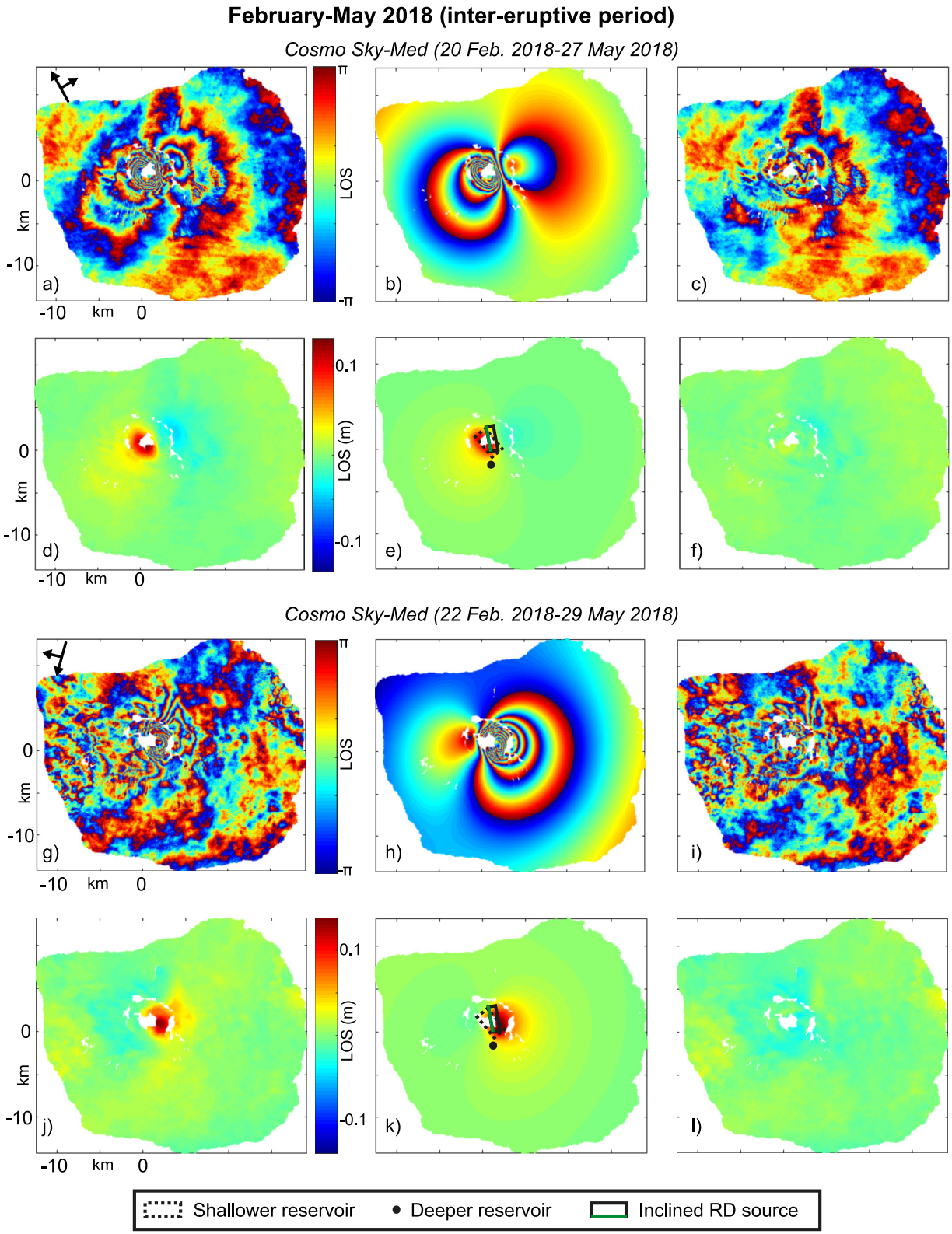

Figure 5. Wrapped (a and g) and unwrapped (d and j) COSMO-SkyMed LOS displacements for the February–May 2018 period (inter-eruptive period). (b, e, h, and k) Predicted displacements (two RD model and one Mogi model) using the MAP solutions. (c, f, i, and l) Related residuals. (a–c and g–i) Each fringe (full color cycle) represents 2π radians of phase change corresponding to 1.55 cm of range change in the LOS direction. (e and k) The black rectangle on model plots represents the outline of the optimal RD plane, with the green thicker line outlining the updip edge of the RD (no green line if the RD is horizontal), while the black dot is the position of the Mogi. The origin for all panels is: −91.55° and −0.3795°.

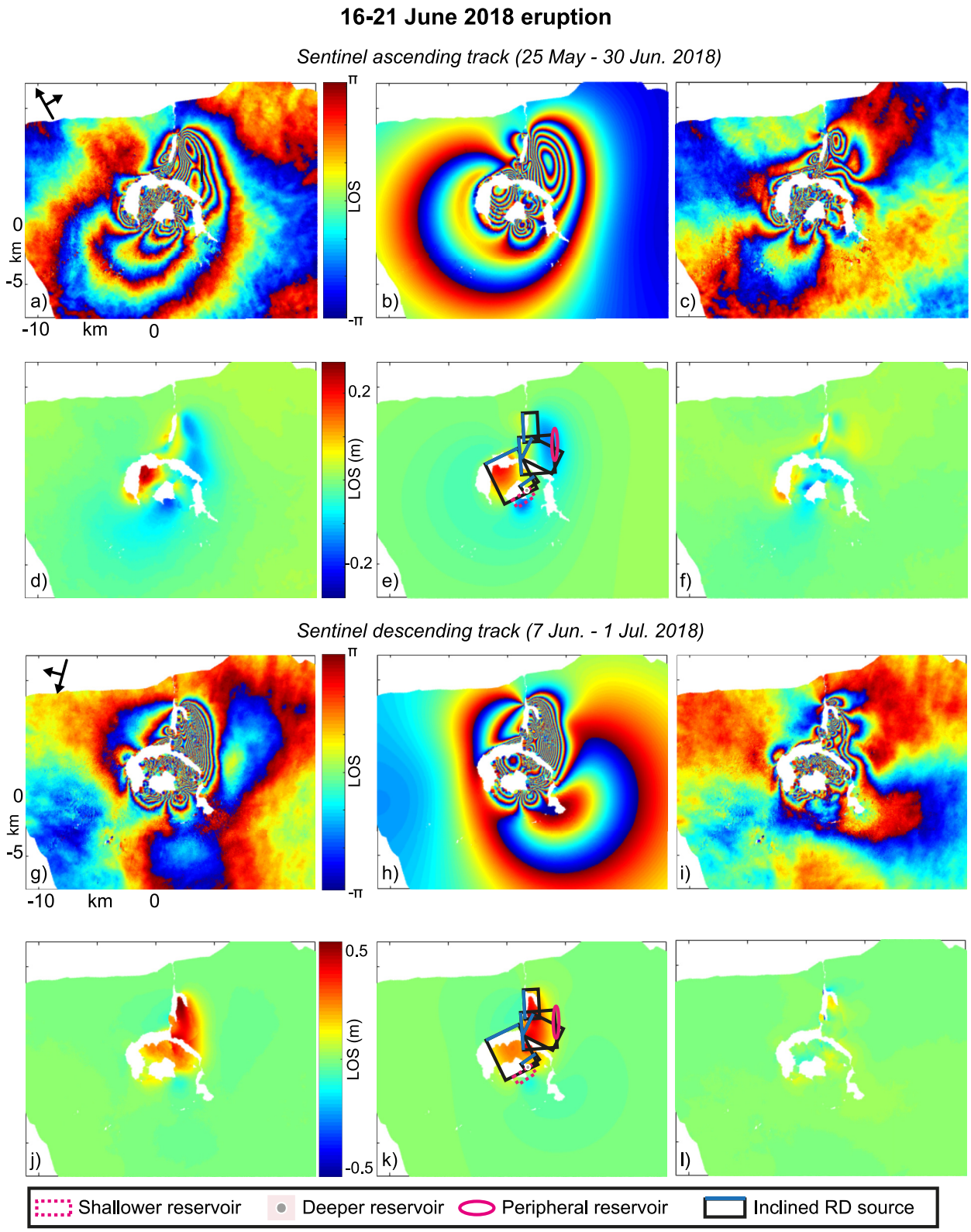

Figure 6. Wrapped (a and g) and unwrapped (d and j) Sentinel-1 displacements for the June 2018 eruption. (b, e, h, and k) Predicted displacements using the MAP solutions. (c, f, i, and l) Related residuals. (a–c and g–i) Each fringe (full color cycle) represents 2π radians of phase change corresponding to 2.8 cm of range change in the LOS direction. (e and k) The rectangles on model plots represent the outline of the optimal RD planes, with the blue thicker line outlining the updip edge of the RD (no blue line if the RD is horizontal), while the gray dot is the position of the Mogi and the ellipse is the ellipsoidal source. The origin for all panels is: −91.55° and −0.3795°.

5.5. July–August 2018 (Post 2018 Eruption)

To model the deformation pattern observed between July and August 2018 (Figure 7), we use a horizontal RD source for the shallow magma reservoir of Fernandina (Bagnardi & Amelung, 2012; Chadwick et al., 2011) and an inclined RD source (dike-like source) (Figure 7). The horizontal RD source (sill-like) converges to a 3.3×1.8 km horizontal sill with volume change of $8.60 \pm 0.37 \times 10^5$ m^3 (Table S7). As for the inclined dike, the Bayesian analysis converges to a 2.2×0.6 km inclined dike (dip angle ~80°), whose top is placed below the horizontal sill at a depth of 1.3 ± 0.1 km below the surface, with volume change of $1.15 \pm 0.12 \times 10^6$ m^3 (Table S7). No contribution from the deep reservoir is required to fit the data.

5.6. September 2018–January 2019 (Post 2018 Eruption)

To model the deformation pattern observed from September 2018 to January 2019, we use an inflating horizontal RD source and an inflating horizontal ellipsoid (Yang's source) for the shallower and the deeper magma reservoirs, respectively (Figure 8; Bagnardi & Amelung, 2012; Bagnardi et al., 2013). To reduce the number of variables, we fixed the geometry of the Yang source according to Bagnardi and Amelung (2012) (see Table S8). The horizontal RD source (sill-like) converges to a 2.6×1.3 km horizontal sill with volume change of $6.48 \pm 0.35 \times 10^5$ m^3 (Figure 8; Table S8). As for the Yang's source, the Bayesian analysis converges to a positive volume change of $5.14 \pm 0.53 \times 10^6$ m^3 (Table S8), obtained using the formula in Tiampo et al. (2000).

6. Discussion

6.1. The September 2017 Eruption

The InSAR observations and geodetic modeling allow us to reconstruct the behavior of Fernandina from September 2017 to January 2019. The propagation of a circumferential dike to the surface triggered the September 2017 eruption. To model the observed deformation, we used the geometry of a circumferential dike propagating from a slightly inclined sill (26°) that probably originated from the shallow magma reservoir (Figure 9a). This geometry is consistent with the model used by Chadwick et al. (2011) for the 2005 circumferential eruption in the same area, suggesting a similar mechanism for these two eruptions. Another similarity between the 2005 and 2017 eruptions is that most of the subsidence is due to the deflation of the deep magma reservoir (Chadwick et al., 2011). On the other hand, the main difference is that an additional vertical dike, with positive volume change, is needed in between the two magma reservoirs to reduce the residuals in our modeling. This suggests an efficient mechanism of magma transfer from the deeper to the shallower reservoir (Figure 9a) and, then, to the surface during the eruption. The total added volume of the two RD sources used for modeling the circumferential dike plus that of the deep dike is $9.65 \pm 0.93 \times 10^6$ m^3 (Table S9). As the shallow reservoir experienced negligible deflation, this volume is similar to the volume lost by the deep magma reservoir ($-9.71 \pm 1.38 \times 10^6$ m^3) and to the erupted volume ($9.7 \pm 4.9 \times 10^6$ m^3 DRE; Vasconez et al., 2018). Assuming that the dikes volume represents the amount of intruded magma, the total volume of intruded plus erupted magma is roughly twice the volume lost by the deep reservoir. This unbalance could be due to the presence of a compressible magma in the deep reservoir (Edmonds & Woods, 2018; Rivalta & Segall, 2008; Yip et al., 2022), or to the fact that the deep reservoir was partly replenished by new magma during the eruption. There is currently no means to discriminate between these two possibilities.

Finally, it is worth noting that the location of this eruption was anticipated by Bagnardi et al. (2013) considering the stress changes produced by the previous 2009 radial eruption. Thus, the location of this eruption supports the idea that the stress changes due to previous intrusions can influence the location of the following eruption, resulting in an alternation of radial and circumferential intrusions on the same side of the volcano (Bagnardi et al., 2013; Chadwick & Dieterich, 1995).

6.2. Inter-Eruptive Period

From December 2017 to February 2018, the deep magma reservoir inflated, recovering most of the volume lost during the 2017 eruption ($7.48 \pm 0.78 \times 10^6$ m^3) (Figure 9b and Figure S8 in Supporting Information S1), with an average inflow rate of magma of $3.41 \pm 0.36 \times 10^7$ m^3/year. This is an order of magnitude higher than that observed in the year after the 2005 eruption (Chadwick et al., 2011) and similar to that observed at Fernandina

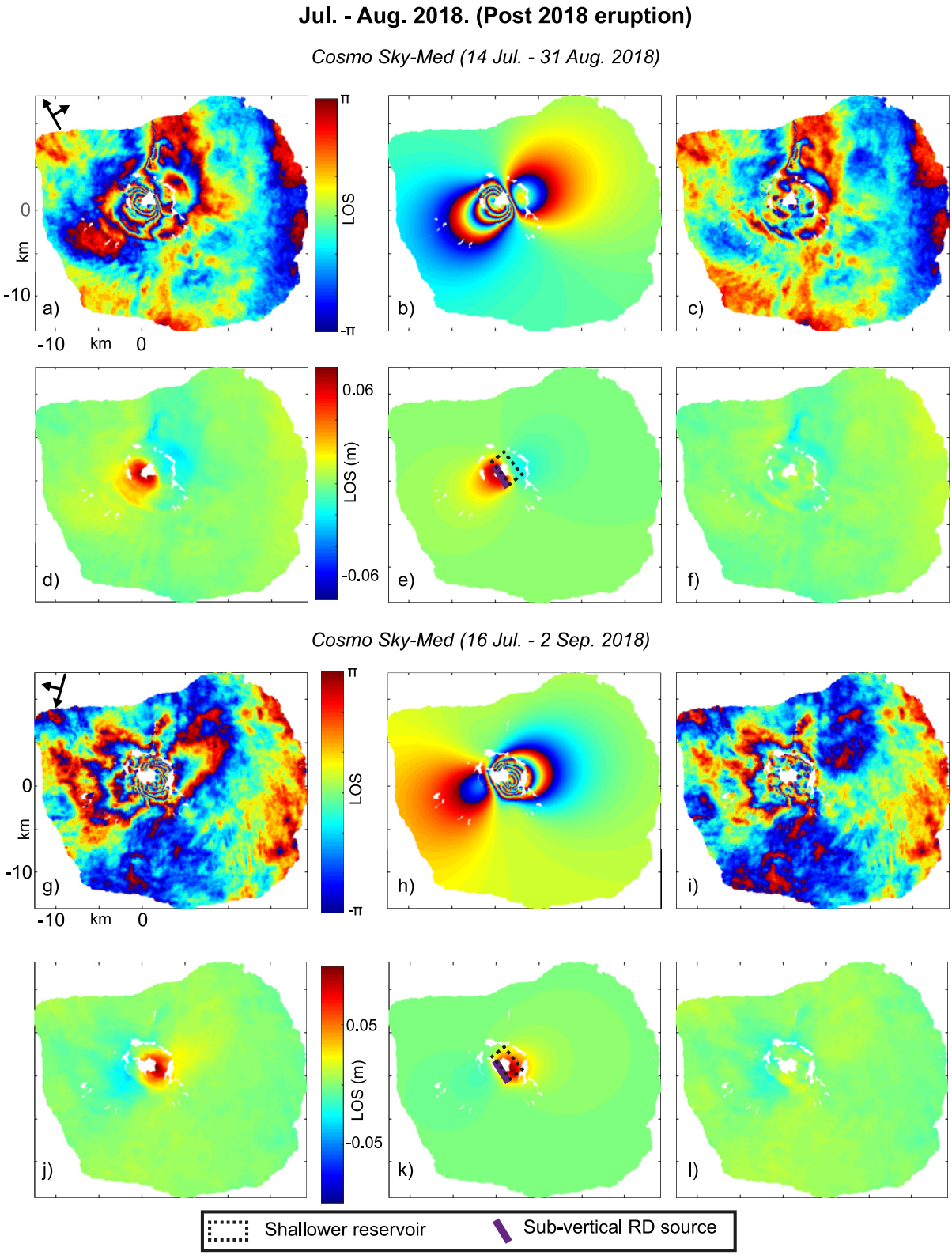

Figure 7. Wrapped (a and g) and unwrapped (d and j) displacements for the July–August 2018 period. (b, e, h, and k) Predicted displacements (two RD model) using the MAP solutions. (c, f, i, and l) Related residuals. (a–c and g–i) Each fringe (full color cycle) represents 2π radians of phase change corresponding to 1.55 cm of range change in the LOS direction. (e and k) The rectangle on model plots represents the outline of the optimal horizontal RD plane, with the purple thicker line outlining the updip edge of the sub-vertical RD source. The origin for all panels is: −91.55° and −0.3795°.

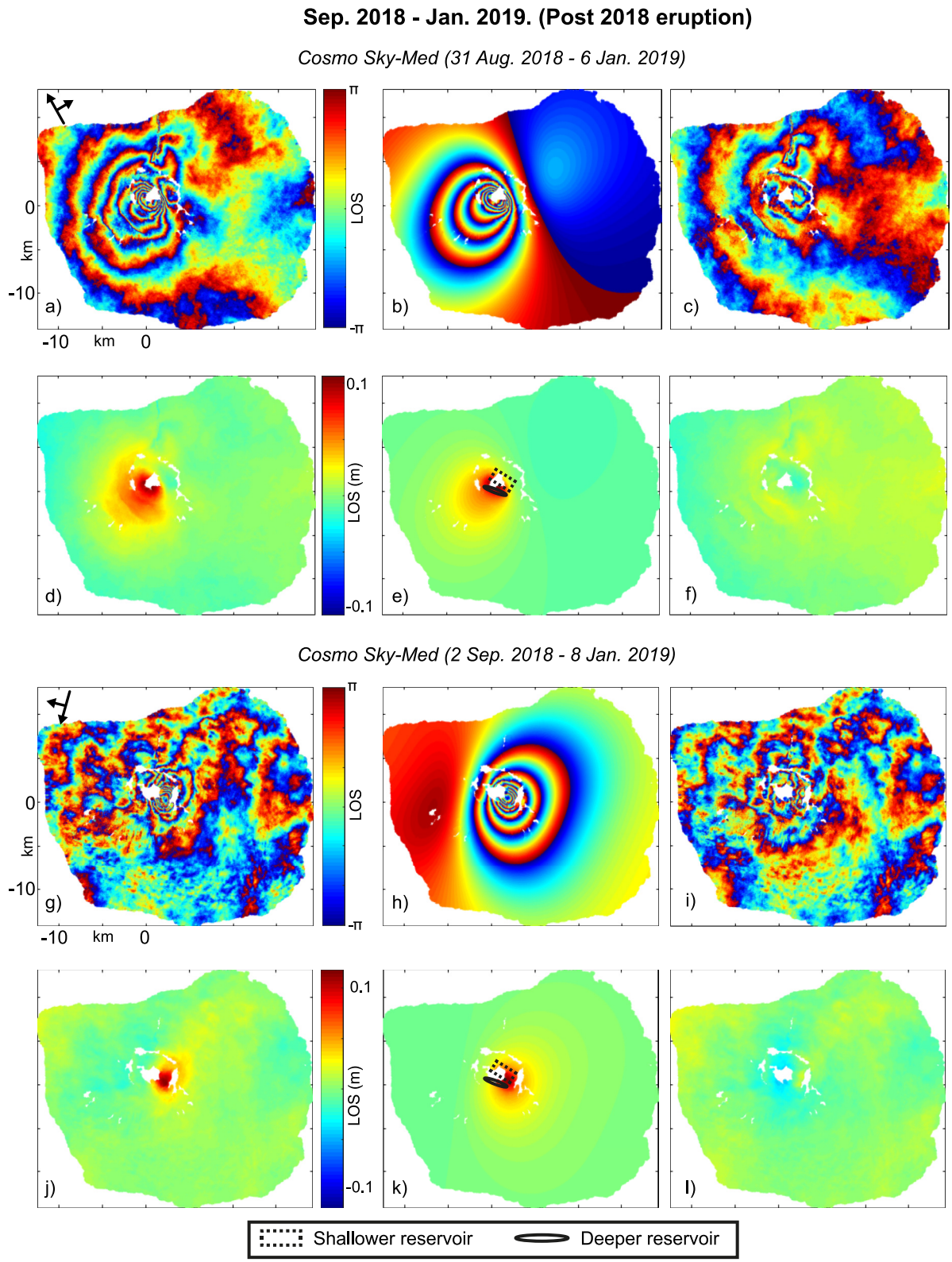

Figure 8. Wrapped (a and g) and unwrapped (d and j) displacements for the September 2018–January 2019 period. (b, e, h, and k) Predicted displacements (one RD and one Yang model) using the MAP solutions (MAP). (c, f, i, and l) Related residuals. (a–c and g–i) Each fringe (full color cycle) represents 2π radians of phase change corresponding to 1.55 cm of range change in the LOS direction. (e and k) The rectangle and the ellipse on model plots represent the outline of the optimal horizontal RD plane and of the optimal Yang source, respectively. The origin for all panels is: −91.55° and −0.3795°.

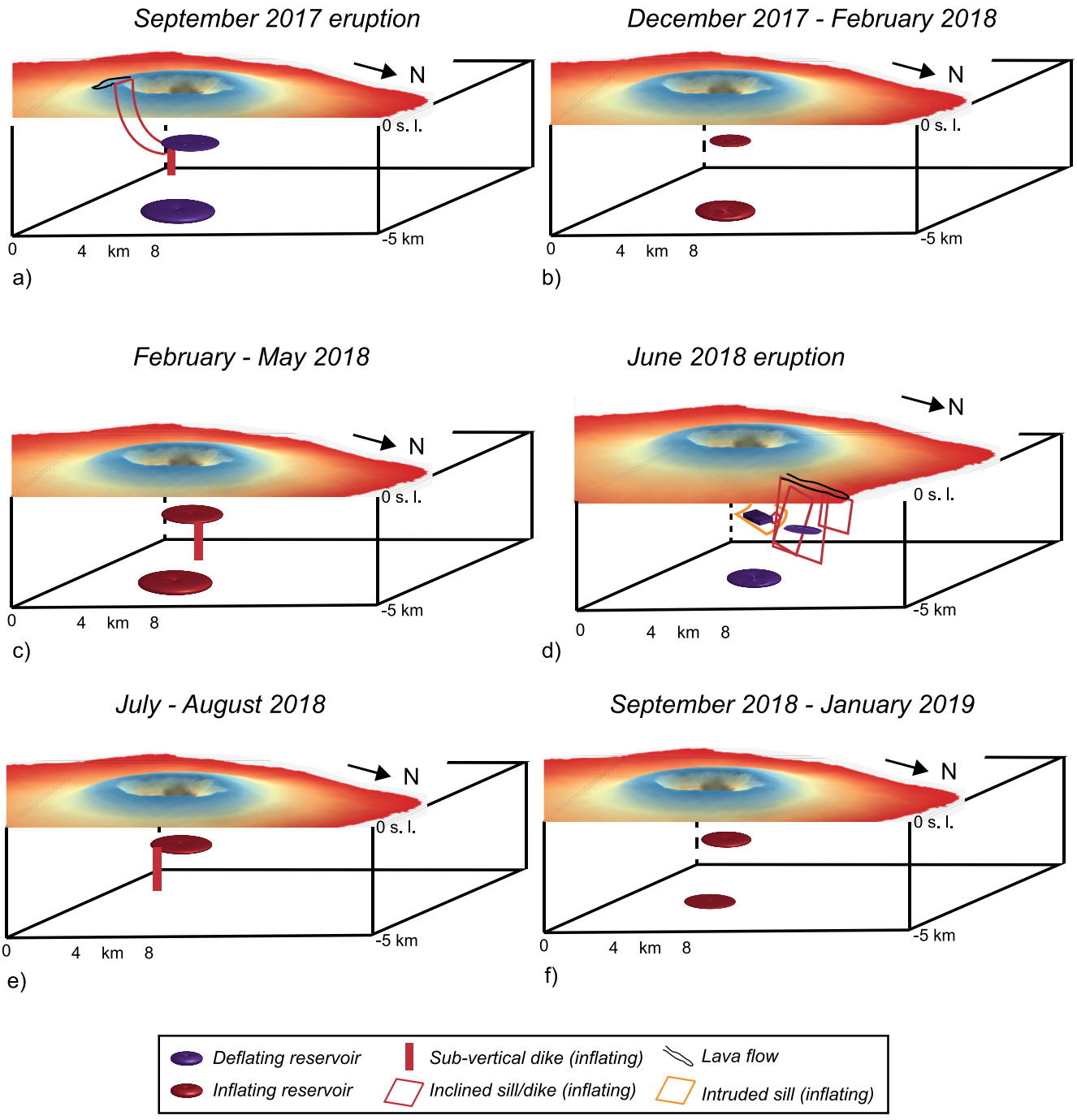

Figure 9. Conceptual models summarizing the sources during the six analyzed time periods of surface deformation at Fernandina. (a) September 2017 eruption. (b and c) inter-eruptive inflation. (d) 2018 eruption. (e and f) post 2018 eruption.

from the end of September 2007 to April 2008, after which a sill propagated from the deep reservoir (Bagnardi & Amelung, 2012). As for the shallow reservoir, it barely inflated ($0.265 \pm 0.035 \times 10^6$ m^3) with low inflow rates of $1.21 \pm 0.16 \times 10^6$ m^3/year, which is the typical inflow rate of the shallow magma reservoir of Fernandina (Bagnardi & Amelung, 2012; Chadwick et al., 2011).

From the end of February 2018 to May 2018, we observed a change in the deformation pattern (Figures 2 and 5). Modeling results suggest a decrease in the magma inflow rate in the deeper reservoir, to $1.2 \pm 0.3 \times 10^7$ m^3/year, and an increase in the magma inflow rate in the shallower reservoir, to $4 \pm 0.2 \times 10^6$ m^3/year. However,

the apparent reduction of the inflow rate to the deeper reservoir could be due to other mechanisms. For example, the uplift signal recorded immediately after the 2017 eruption, mainly modeled with the inflation of the deeper reservoir, could be due to the poro-viscoelastic response of the host rock rather than to a new magma inflow, if the magma in the deeper reservoir is sufficiently incompressible relative to the surrounding crust (Segall, 2019). Alternatively, the stronger deformation signal from the shallower reservoir may mask the activity of the deeper source, as for example, suggested for Campi Flegrei (e.g., Amoruso et al., 2017).

Part of the deformation that occurred from the end of February 2018 to May 2018 has been modeled with the inflation of a vertical dike, whose top is coincident with (or slightly higher than) the depth of the shallower magma reservoir and probably represents a dike that was transferring magma from the deeper to the shallower reservoir (Figure 9c).

6.3. The June 2018 Eruption

The June 2018 eruption shows significant differences with the other recent radial eruptions at Fernandina (1995 and 2009). First, the 2018 radial eruption occurred on the north flank, while the 1995 and the 2009 radial eruptions occurred on the SW flank. This shows that the pattern of alternation between radial and circumferential intrusions on the same side of the volcano (Bagnardi et al., 2013) can be interrupted by intrusions on the opposite side of the volcano. Second, the 2018 deformation on the north flank is characterized by a peculiar asymmetric fringe pattern, with the eastern fringes associated with the radial dike showing a straight, non curvilinear, geometry (Figures 6a and 6g). This is different from what was observed in 2009 on the SW flank, which was characterized by the curvilinear fringes (Bagnardi et al., 2013) typical of most dikes (Lisowski, 2007). Third, the LOS displacements are opposite in sign in the ascending and descending tracks (Figure 6), but with a significant change in magnitude that is difficult to reproduce by using RD sources only. For these reasons, we were unable to fully model this complex deformation pattern simply by using inclined RD sources. Instead, we had to use four inflating RD sources and a deflating Yang source (Figure 9d). For the RD sources, three of them represent the radial dike that propagated, probably from the shallow reservoir, as a slightly inclined sill and then increased its inclination upward while twisting around a radial axis, similar to the model proposed by Bagnardi et al. (2013). However, when the dike propagated outside the caldera, it apparently bifurcated, generating a new splay that propagated toward NE (Figures 6b and 6h). Immediately to the east of this second dike, at the depth of its mid-to-lower portion, is located the deflating Yang source (Figures 6 and 9d), which could represent a small peripheral melt (or mush) pocket that was intersected and drained by the dike. The lack of additional complementary information (e.g., petrological data) does not allow us to test this hypothesis, so for the moment it remains speculative.

Another feature of this eruption is the apparent propagation of an inclined sheet toward the NNW (Figure 6) that did not reach the surface (stalling at 800 m depth). Complex magma propagation in multiple directions has been inferred at a few other basaltic shields with summit calderas, like Ambrym (Shreve et al., 2021) and perhaps Cerro Azul (Galetto et al., 2020). However, InSAR data from Galápagos volcanoes suggest that laterally propagating sills emplaced at different depth (from 2 to 6 km) without erupting, at Fernandina in 2007 (Bagnardi & Amelung, 2012), at Cerro Azul in 2017 (Guo et al., 2019) and at Alcedo in 2010 (Galetto et al., 2019). Conversely, a laterally propagating sill triggered the 2018 eruption at Sierra Negra (Davis et al., 2021).

Similar to the 2017 eruption and to the other previous eruptions at Fernandina (2005, 2009) most of the magma was lost from the deeper reservoir (Figure S8 in Supporting Information S1; Chadwick et al., 2011; Bagnardi et al., 2013). Sentinel-1 data show that the volume lost by the deep reservoir is $-13.1 \pm 0.5 \times 10^6$ m^3. The total volume of all the modeled RD sources is $12.3 \pm 0.4 \times 10^6$ m^3 (Tables S5 and S9). By adding the erupted volume ($5.9 \pm 3 \times 10^6$ m^3 DRE; Vasconez et al., 2018) to the volume of the RD sources, the total intruded plus erupted volume is 18.2 ± 3.35 m^3, quite consistent with the total volume lost by all the deflating sources (-15.2 ± 0.63 m^3). The CSK data also show that most of the magma was lost from the deep magma reservoir ($-9.09 \pm 0.41 \times 10^6$ m^3). This volume is lower than that of all the RD sources ($12.15 \pm 0.38 \times 10^6$ m^3), but this discrepancy is compensated by the volume lost by the Yang source and the shallow reservoir, which are larger than those estimated from Sentinel-1 data (especially the Yang source). The total volume lost by the three deflating sources is $-11.69 \pm 0.73 \times 10^6$ m^3 (Tables S6 and S9). Variations in the volume change of the Mogi source between the Sentinel-1 and the CSK model results might be due to the different acquisition times between the two datasets, with the CSK data covering a smaller time interval and perhaps having better resolution during the syn-eruptive period. The total intruded plus erupted volumes from CSK data are 18.05 ± 3.38 m^3, which is from

15% to 49% higher than the volumes lost by all the deflating sources. This unbalance is lower than that observed in 2017, suggesting a less compressible magma (Rivalta & Segall, 2008) or a lower supply of magma in the deep reservoir during the 2018 eruption. Finally, the intruded volume during the 2018 eruption is roughly twice the erupted volume, suggesting that this event has been mainly intrusive. This fact potentially explains why the 2018 radial eruption produced about an order of magnitude less magma than that erupted during the 2009 radial eruption, during which the erupted volume was larger than the intruded one (Bagnardi et al., 2013; Vasconez et al., 2018).

6.4. After the June 2018 Eruption

The shallow magma reservoir continued to inflate, with an average inflow rate of $6.54 \pm 0.2 \times 10^6$ m^3/year, from July to the end of August. This inflow rate is slightly higher than those observed after the 2017 eruption (see above), although within the same order of magnitude. Our modeling results suggest that a sub-vertical dike was feeding the shallow magma reservoir during its inflation (Figure 9e), although we do not observe any signal related to the deep magma reservoir. This could be due to the fact that the deep reservoir was being fed at about the same rate, experiencing no net deformation. From September 2018 to January 2019, the inflow rate into the shallow magma reservoir decreased to $1.85 \pm 0.1 \times 10^6$ m^3/year. At the same time, the deeper magma reservoir inflated again, with an average rate of $1.47 \pm 0.15 \times 10^7$ m^3/year (Figure 9f). These rates are similar to those observed after the 2017 eruption. Further studies could investigate whether magma supply to the two reservoirs continued after January 2019 (the end of our InSAR time series) and their possible role in the January 2020 circumferential eruption.

6.5. Deep Versus Shallow Reservoir

Our data suggest that Fernandina has two hydraulically connected magma reservoirs, with magma being transferred (either through porous flow within a crystal mush or viscous flow in a conduit) from a deeper to a shallower reservoir during both eruptive and inter-eruptive periods (Bagnardi & Amelung, 2012; Chadwick et al., 2011).

Results from the inversion of geodetic data suggest that the volume of magma that accumulates in the deeper reservoir is often higher than in the shallower reservoir during the inter-eruptive periods at Fernandina (Table S9 and Figure S8 in Supporting Information S1; Chadwick et al., 2011; Bagnardi & Amelung, 2012). This suggests that magma mainly accumulates within the deep reservoir, with just a portion being transferred in the shallower reservoir, similar to what is suggested for Wolf volcano (Stock et al., 2018). During the 2017 and 2018 eruptions, our modeling data suggest a rapid and efficient magma transfer from the deeper to the shallower reservoir and then to the sills/dikes, again similar to what suggested for Wolf volcano (Stock et al., 2018; Xu et al., 2016). This transfer could have started in the hours just before the two analyzed eruptions, as previously found for the 2009 eruption (Bagnardi et al., 2013), although the temporal resolution of our InSAR data does not allow to confirm this hypothesis. This interpretation would be consistent with the results in Galetto et al. (2022) that suggest that magma inflow rates $<10^7$ m^3/year, like those associated with the shallow reservoir at Fernandina from December 2017 to May 2018 and from July 2018 to January 2019, would not be high enough for reaching a critical overpressure threshold in this reservoir to nucleate a dike.

The observed syn- and inter-eruptive behaviors at Fernandina suggest a difference to what happens at Sierra Negra volcano, where geodetic signals are mainly related to the accumulation of magma in the shallow reservoir, usually at higher rates, during inter-eruptive periods and to the withdrawal of magma from the shallow reservoir during eruptions (Bell, Hernandez, et al., 2021; Chadwick et al., 2006; Geist et al., 2006, 2008; Gregg et al., 2018, 2022). No geodetic signal associated with a deeper reservoir has been observed at Sierra Negra in the last 30 years, although petrological data support its existence, showing for example that a portion of the magma erupted in 2018 equilibrated at a depth of 7.5 ± 2.9 km (Bell, La Femina, et al., 2021; Reynolds & Geist, 1995).

The significant role of the deeper magmatic reservoirs at both Fernandina and Wolf volcanoes, highlighted by geodetic data, might be related to their similar evolutionary stage, different from the more mature and evolved Sierra Negra (Geist et al., 2014; Harpp & Geist, 2018). In fact, the compositionally monotonous volcanoes of Fernandina and Wolf are in a younger steady state phase and seem characterized by a primary role of the deeper reservoir in accumulating magma and transferring it to the shallower reservoir, possibly controlling the eruptions. Conversely the more mature volcano of Sierra Negra can erupt more evolved and cooler magma

usually accumulating in the shallow reservoir, which might have a more important role in controlling eruptions (Chadwick et al., 2006; Geist et al., 2008; Gregg et al., 2022).

7. Conclusions

The 2017 eruption at Fernandina volcano was similar to the 2005 eruption, both in the position of the eruptive fissures and the geometry of the circumferential feeder dike. Following that eruption, two successive episodes of magma inflow occurred in the deep and shallow magma reservoirs. The subsequent radial eruption in June 2018 differed from the 2009 radial eruption, by occurring in a different location (the north flank), by a splaying of the radial dike, by its possible interaction with a peripheral melt pocket, and by intruding a lateral sill in the NNW sector of the caldera. Inter-eruptive periods were characterized by magma accumulation mainly in the deeper reservoir, while both eruptions seem characterized by sudden and rapid magma transfer from the deeper to the shallower one, suggesting an important role of the deeper reservoir during the eruptions. This is similar to Wolf volcano, and unlike what is observed at Sierra Negra, where the shallower reservoir accumulates higher volumes of magma. These differences in the pre-eruptive role of the deeper and shallow reservoir may be connected with the different evolutionary stages of Fernandina and Wolf with regard to the more mature Sierra Negra.

Data Availability Statement

All the data have been deposited in a permanent data repository and are freely available at: https://doi.org/10.17605/OSF.IO/3ZXY9. Sentinel-1 data were provided through the Copernicus Program of the European Union. Landsat 8 image in Figure 1c is freely distributed by the USGS from https://earthexplorer.usgs.gov/.

Acknowledgments
We are grateful to William W. Chadwick and Dennis Geist for their precise reviews and for their comments and suggestions that significantly improved the quality of this manuscript. COSMO-SkyMed data have been provided by Italian Space Agency (ASI) through the CEOS Volcano Demonstrator—https://ceos.org/ourwork/workinggroups/disasters/volcanoes/ (accessed on 31 August 2022). The authors wish to thank Simona Zoffoli of ASI for her continuous support with the CSK data planning and acquisition. The TanDEM-X DEM exploited in the InSAR processing and in Figures 2, 3, and 10 was provided by the German Aerospace Center (DLR) within the CEOS Volcano Demonstrator. FG was partially supported by a NASA Grant 80NSSC20K1674 from the Interdisciplinary Science Program of the Earth Science Division.

References

Amelung, F., Jónsson, S., Zebker, H., & Segall, P. (2000). Widespread uplift and 'trapdoor' faulting on Galapagos volcanoes observed with radar interferometry. *Nature*, *407*(6807), 993–996. https://doi.org/10.1038/35039604

Amoruso, A., Crescentini, L., D'Antonio, M., & Acocella, V. (2017). Thermally-assisted magma emplacement explains restless calderas. *Scientific Reports*, *7*(1), 7948. https://doi.org/10.1038/s41598-017-08638-y

Bagnardi, M., & Amelung, F. (2012). Space-geodetic evidence for multiple magma reservoirs and subvolcanic lateral intrusions at Fernandina Volcano, Galápagos Islands. *Journal of Geophysical Research*, *117*(B10). https://doi.org/10.1029/2012JB009465

Bagnardi, M., Amelung, F., & Poland, M. P. (2013). A new model for the growth of basaltic shields based on deformation of Fernandina volcano, Galápagos Islands. *Earth and Planetary Science Letters*, *377*, 358–366. https://doi.org/10.1016/j.epsl.2013.07.016

Bagnardi, M., & Hooper, A. (2018). Inversion of surface deformation data for rapid estimates of source parameters and uncertainties: A Bayesian approach. *Geochemistry, Geophysics, Geosystems*, *19*(7), 2194–2211. https://doi.org/10.1029/2018GC007585

Bell, A. F., Hernandez, S., Femina, P. C. L., & Ruiz, M. C. (2021). Uplift and seismicity driven by magmatic inflation at Sierra Negra Volcano, Galápagos Islands. *Journal of Geophysical Research: Solid Earth*, *126*, e2021JB022244. https://doi.org/10.1029/2021JB022244

Bell, A. F., La Femina, P. C., Ruiz, M., Amelung, F., Bagnardi, M., Bean, C. J., et al. (2021). Caldera resurgence during the 2018 eruption of Sierra Negra volcano, Galápagos Islands. *Nature Communications*, *12*(1), 1397. https://doi.org/10.1038/s41467-021-21596-4

Berardino, P., Fornaro, G., Lanari, R., & Sansosti, E. (2002). A new algorithm for surface deformation monitoring based on small baseline differential SAR interferograms. *IEEE Transactions on Geoscience and Remote Sensing*, *40*(11), 2375–2383. https://doi.org/10.1109/TGRS.2002.803792

Bernard, B., Ramón, P., García, L., Hernandez, S., Vasconez, F. J., Viracucha, G., & Hidalgo, S. (2022). Volcanic event management in the Galápagos Islands, Ecuador. *Volcanica*, *5*(1), 209–225. https://doi.org/10.30909/vol.05.01.209225

Chadwick, W. W., Jónsson, S., Geist, D. J., Poland, M., Johnson, D. J., Batt, S., et al. (2011). The May 2005 eruption of Fernandina volcano, Galápagos: The first circumferential dike intrusion observed by GPS and InSAR. *Bulletin of Volcanology*, *73*(6), 679–697. https://doi.org/10.1007/s00445-010-0433-0

Chadwick, W. W., Jr., Geist, D. J., Jónsson, S., Poland, M., Johnson, D. J., & Meertens, C. M. (2006). A volcano bursting at the seams: Inflation, faulting, and eruption at Sierra Negra Volcano, Galápagos. *Geology*, *34*(12), 1025–1028. https://doi.org/10.1130/G22826A.1

Chadwick, W. W., Jr., & Howard, K. A. (1991). The pattern of circumferential and radial eruptive fissures on the volcanoes of Fernandina and Isabela Islands, Galapagos. *Bulletin of Volcanology*, *53*(4), 259–275. https://doi.org/10.1007/BF00414523

Chadwick, W. W., Jr., & Dieterich, J. H. (1995). Mechanical modeling of circumferential and radial dike intrusion on Galápagos volcanoes. *Journal of Volcanology and Geothermal Research*, *66*(1–4), 37–52. https://doi.org/10.1016/0377-0273(94)00060-T

Chestler, S. R., & Grosfils, E. B. (2013). Using numerical modeling to explore the origin of intrusion patterns on Fernandina volcano, Galapagos Islands, Ecuador. *Geophysical Research Letters*, *40*(17), 4565–4569. https://doi.org/10.1002/grl.50833

Corbi, F., Rivalta, E., Pinel, V., Maccaferri, F., & Acocella, V. (2016). Understanding the link between circumferential dikes and eruptive fissures around calderas based on numerical and analog models. *Geophysical Research Letters*, *43*(12), 6212–6219. https://doi.org/10.1002/2016GL068721

Corbi, F., Rivalta, E., Pinel, V., Maccaferri, F., Bagnardi, M., & Acocella, V. (2015). How caldera collapse shapes the shallow emplacement and transfer of magma in active volcanoes. *Earth and Planetary Science Letters*, *431*, 287–293. https://doi.org/10.1016/j.epsl.2015.09.028

Davis, T., Bagnardi, M., Lundgren, P., & Rivalta, E. (2021). Extreme curvature of shallow magma pathways controlled by competing stresses: Insights from the 2018 Sierra Negra eruption. *Geophysical Research Letters*, *48*(13), e2021GL093038. https://doi.org/10.1029/2021GL093038

Decriem, J., Árnadóttir, T., Hooper, A., Geirsson, H., Sigmundsson, F., Keiding, M., et al. (2010). The 2008 May 29 earthquake doublet in SW Iceland. *Geophysical Journal International*, *181*, 1128–1146. https://doi.org/10.1111/j.1365-246X.2010.04565.x

Dumont, Q., Cayol, V., Froger, J. L., & Peltier, A. (2022). 22 years of satellite imagery reveal a major destabilization structure at Piton de la Fournaise. *Nature Communications*, *13*, 1–11. https://doi.org/10.1038/s41467-022-30109-w

Edmonds, M., & Woods, A. W. (2018). Exsolved volatiles in magma reservoirs. *Journal of Volcanology and Geothermal Research*, *368*, 13–30. https://doi.org/10.1016/j.jvolgeores.2018.10.018

Feighner, M. A., & Richards, M. A. (1994). Lithospheric structure and compensation mechanisms of the Galápagos Archipelago. *Journal of Geophysical Research*, *99*(B4), 6711–6729. https://doi.org/10.1029/93JB03360

Fornaro, G., Pauciullo, A., & Reale, D. (2011). A null-Space method for the phase unwrapping of multitemporal SAR Interferometric stacks. *IEEE Transactions on Geoscience and Remote Sensing*, *49*(6), 2323–2334. https://doi.org/10.1109/TGRS.2010.2102767

Gaete, A., Kavanagh, J. L., Rivalta, E., Hazim, S. H., Walter, T. R., & Dennis, D. J. (2019). The impact of unloading stresses on post-caldera magma intrusions. *Earth and Planetary Science Letters*, *508*, 109–121. https://doi.org/10.1016/j.epsl.2018.12.016

Galetto, F., Acocella, V., Hooper, A., & Bagnardi, M. (2022). Eruption at basaltic calderas forecast by magma flow rate. *Nature Geoscience*, *15*(7), 580–584. https://doi.org/10.1038/s41561-022-00960-z

Galetto, F., Bagnardi, M., Acocella, V., & Hooper, A. (2019). Noneruptive unrest at the Caldera of Alcedo Volcano (Galápagos Islands) revealed by InSAR data and geodetic modeling. *Journal of Geophysical Research: Solid Earth*, *124*(4), 3365–3381. https://doi.org/10.1029/2018JB017103

Galetto, F., Hooper, A., Bagnardi, M., & Acocella, V. (2020). The 2008 eruptive unrest at Cerro Azul volcano (Galápagos) revealed by InSAR data and a novel method for geodetic modelling. *Journal of Geophysical Research: Solid Earth*, *125*(2), e2019JB018521. https://doi.org/10.1029/2019JB018521

Galetto, F., Pritchard, M. E., Hornby, A. J., Gazel, E., & Mahowald, N. M. (2023). Spatial and temporal quantification of subaerial volcanism from 1980 to 2019: Solid products, masses and average eruptive rates. *Reviews of Geophysics*, *61*(1), e2022RG000783. https://doi.org/10.1029/2022RG000783

Geist, D., Chadwick, W., & Johnson, D. (2006). Results from new GPS and gravity monitoring networks at Fernandina and Sierra Negra Volcanoes, Galápagos, 2000–2002. *Journal of Volcanology and Geothermal Research*, *150*(1–3), 79–97. https://doi.org/10.1016/j.jvolgeores.2005.07.003

Geist, D. J., Bergantz, G., & Chadwick, W. W., Jr. (2014). Galápagos magma chambers. In K. S. Harpp, E. Mittelstaedt, N. d'Ozouville, & D. W. Graham (Eds.), *The Galápagos: A natural Laboratory for the Earth Sciences* (Vol. 204, pp. 55–70). John Wiley & Sons.

Geist, D. J., Harpp, K. S., Naumann, T. R., Poland, M., Chadwick, W. W., Hall, M., & Rader, E. (2008). The 2005 eruption of Sierra Negra volcano, Galápagos, Ecuador. *Bulletin of Volcanology*, *m70*(6), 655–673. https://doi.org/10.1007/s00445-007-0160-3

Gibson, S. A., & Geist, D. (2010). Geochemical and geophysical estimates of lithospheric thickness variation beneath Galápagos. *Earth and Planetary Science Letters*, *300*(3–4), 275–286. https://doi.org/10.1016/j.epsl.2010.10.002

Global Volcanism Program. (2013). *Volcanoes of the world*. Distributed by Smithsonian Institution, compiled by Venzke, E. https://doi.org/10.5479/si.GVP.VOTW5-2022.5.0

Gregg, P. M., Le Mével, H., Zhan, Y., Dufek, J., Geist, D., & Chadwick, W. W., Jr. (2018). Stress triggering of the 2005 eruption of Sierra Negra Volcano, Galápagos. *Geophysical Research Letters*, *45*(24), 13–288. https://doi.org/10.1029/2018GL080393

Gregg, P. M., Zhan, Y., Amelung, F., Geist, D., Mothes, P., Koric, S., & Yunjun, Z. (2022). Forecasting mechanical failure and the 26 June 2018 eruption of Sierra Negra Volcano, Galápagos, Ecuador. *Science Advances*, *8*(22), eabm4261. https://doi.org/10.1126/sciadv.abm4261

Guo, Q., Xu, C., Wen, Y., Liu, Y., & Xu, G. (2019). The 2017 noneruptive unrest at the Caldera of Cerro Azul Volcano (Galápagos Islands) revealed by InSAR observations and geodetic modelling. *Remote Sensing*, *11*(17), 1992. https://doi.org/10.3390/rs11171992

Harpp, K. S., & Geist, D. J. (2018). The evolution of Galápagos Volcanoes: An alternative prospective. *Frontiers of Earth Science*, *6*, 50. https://doi.org/10.3389/feart.2018.00050

Hooft, E. E., Toomey, D. R., & Solomon, S. C. (2003). Anomalously thin transition zone beneath the Galápagos hotspot. *Earth and Planetary Science Letters*, *216*(1–2), 55–64. https://doi.org/10.1016/S0012-821X(03)00517-X

Howard, K. A., Simkin, T., Geist, D. J., Merlen, G., & Nolf, B. (2019). Large hydromagmatic eruption related to Fernandina Volcano's 1968 caldera collapse—Deposits, landforms, and ecosystem recovery. https://doi.org/10.1130/2018.2538(18)

Jónsson, S., Zebker, H., Cervelli, P., Segall, P., Garbeil, H., Mouginis-Mark, P., & Rowland, S. (1999). A shallow-dipping dike fed the 1995 flank eruption at Fernandina Volcano, Galápagos, observed by satellite radar interferometry. *Geophysical Research Letters*, *26*(8), 1077–1080. https://doi.org/10.1029/1999GL900108

Krieger, G., Moreira, A., Fiedler, H., Hajnsek, I., Werner, M., Younis, M., & Zink, M. (2007). TanDEM-X: A satellite formation for high-resolution SAR interferometry. *IEEE Transactions on Geoscience and Remote Sensing*, *45*(11), 3317–3341. https://doi.org/10.1109/TGRS.2007.900693

Lisowski, M. (2007). Analytical volcano deformation source models. In *Volcano deformation* (pp. 279–304). Springer. https://doi.org/10.1007/978-3-540-49302-0_8

Mogi, K. (1958). Relations between the eruptions of various volcanoes and the deformations of the ground surfaces around them. *Bulletin of the Earthquake Research Institute*, *36*, 99–134.

Munro, D. C., & Rowland, S. K. (1996). Caldera morphology in the Western Galápagos and implications for volcano eruptive behavior and mechanisms of caldera formation. *Journal of Volcanology and Geothermal Research*, *72*(1–2), 85–100. https://doi.org/10.1016/0377-0273(95)00076-3

Naumann, T., & Geist, D. (2000). Physical volcanology and structural development of Cerro Azul Volcano, Isabela Island, Galápagos: Implications for the development of Galápagos-type shield volcanoes. *Bulletin of Volcanology*, *61*(8), 497–514. https://doi.org/10.1007/s004450050001

Nikkhoo, M., Walter, T. R., Lundgren, P. R., & Prats-Iraola, P. (2017). Compound dislocation models (CDMs) for volcano deformation analyses. *Geophysical Journal International*, *208*(2), 877–894. https://doi.org/10.1093/gji/ggw427

Okada, Y. (1985). Surface deformation due to shear and tensile faults in a half-space. *Bulletin of the Seismological Society of America*, *75*(4), 1135–1154. https://doi.org/10.1785/bssa0750041135

Peltier, A., Villeneuve, N., Ferrazzini, V., Testud, S., Hassen Ali, T., Boissier, P., & Catherine, P. (2018). Changes in the long-term geophysical eruptive precursors at Piton de la Fournaise: Implications for the response management. *Frontiers of Earth Science*, *6*, 104. https://doi.org/10.3389/feart.2018.00104

Poland, M. P. (2014). Contrasting volcanism in Hawai'i and the Galápagos. In K. S. Harpp, E. Mittelstaedt, N. d'Ozouville, & D. W. Graham (Eds.), *The Galápagos: A Natural Laboratory for the Earth Sciences* (Vol. 204, pp. 5–26). John Wiley & Sons.

Reynolds, R. W., & Geist, D. J. (1995). Petrology of lavas from Sierra Negra Volcano, Isabela Island, Galápagos Archipelago. *Journal of Geophysical Research*, *100*(B12), 24537–24553. https://doi.org/10.1029/95JB02809

Rivalta, E., & Segall, P. (2008). Magma compressibility and the missing source for some dike intrusions. *Geophysical Research Letters*, *35*(4), L04306. https://doi.org/10.1029/2007GL032521

Sansosti, E., Berardino, P., Manunta, M., Serafino, F., & Fornaro, G. (2006). Geometrical SAR image registration. *IEEE Transactions on Geoscience and Remote Sensing*, *44*(10), 2861–2870. https://doi.org/10.1109/TGRS.2006.875787

Segall, P. (2019). Magma chambers: What we can, and cannot, learn from volcano geodesy. *Philosophical Transactions of the Royal Society A*, *377*(2139), 20180158. https://doi.org/10.1098/rsta.2018.0158

Shreve, T., Grandin, R., Smittarello, D., Cayol, V., Pinel, V., Boichu, M., & Morishita, Y. (2021). What triggers caldera ring-fault Subsidence at Ambrym Volcano? Insights from the 2015 dike intrusion and eruption. *Journal of Geophysical Research: Solid Earth*, *126*(6), e2020JB020277. https://doi.org/10.1029/2020JB020277

Simkin, T., & Howard, K. A. (1970). Caldera collapse in the Galapagos Islands, 1968: The largest known collapse since 1912 followed a flank eruption and explosive volcanism within the caldera. *Science*, *169*(3944), 429–437. https://doi.org/10.1126/science.169.3944.429

Smets, B., Kervyn, M., d'Oreye, N., & Kervyn, F. (2015). Spatio-temporal dynamics of eruptions in a youthful extensional setting: Insights from Nyamulagira Volcano (DR Congo), in the Western branch of the East African Rift. *Earth-Science Reviews*, *150*, 305–328. https://doi.org/10.1016/j.earscirev.2015.08.008

Smittarello, D., Smets, B., BarrièreMichellier, C., Oth, A., Shreve, T., Grandin, R., et al. (2022). Precursor-free eruption triggered by edifice rupture at Nyiragongo Volcano. *Nature*, *609*(7925), 83–88. https://doi.org/10.1038/s41586-022-05047-8

Stock, M. J., Bagnardi, M., Neave, D. A., Maclennan, J., Bernard, B., Buisman, I., et al. (2018). Integrated petrological and geophysical constraints on magma system architecture in the Western Galápagos archipelago: Insights from Wolf volcano. *Geochemistry, Geophysics, Geosystems*, *19*(12), 4722–4743. https://doi.org/10.1029/2018GC007936

Stock, M. J., Geist, D., Neave, D. A., Gleeson, M. L., Bernard, B., Howard, K. A., et al. (2020). Cryptic evolved melts beneath monotonous basaltic shield volcanoes in the Galápagos Archipelago. *Nature Communications*, *11*, 1–13. https://doi.org/10.1038/s41467-020-17590-x

Tiampo, K. F., Rundle, J. B., Fernandez, J., & Langbein, J. O. (2000). Spherical and ellipsoidal volcanic sources at Long Valley Caldera, California, using a genetic algorithm inversion technique. *Journal of Volcanology and Geothermal Research*, *102*(3–4), 189–206. https://doi.org/10.1016/S0377-0273(00)00185-2

Vasconez, F. J., Anzieta, J. C., Vásconez Müller, A., Bernard, B., & Ramón, P. (2022). A near real-time and free tool for the preliminary mapping of active lava flows during volcanic crises: The case of hotspot subaerial eruptions. *Remote Sensing*, *14*, 3483. https://doi.org/10.3390/rs14143483

Vasconez, F. J., Ramón, P., Hernandez, S., Hidalgo, S., Bernard, B., Ruiz, M., et al. (2018). The different characteristics of the recent eruptions of Fernandina and Sierra Negra volcanoes (Galápagos, Ecuador). *Volcanica*, *1*(2), 127–133. https://doi.org/10.30909/vol.01.02.127133

Villagómez, D. R., Toomey, D. R., Geist, D. J., Hooft, E. E., & Solomon, S. C. (2014). Mantle flow and multistage melting beneath the Galápagos hotspot revealed by seismic imaging. *Nature Geoscience*, *7*(2), 151–156. https://doi.org/10.1038/NGEO2062

White, W. M., McBirney, A. R., & Duncan, R. A. (1993). Petrology and geochemistry of the Galápagos Islands: Portrait of a pathological mantle plume. *Journal of Geophysical Research*, *98*(B11), 19533–19563. https://doi.org/10.1029/93JB02018

Xu, W., Jónsson, S., Ruch, J., & Aoki, Y. (2016). The 2015 Wolf volcano (Galápagos) eruption studied using Sentinel-1 and ALOS-2 data. *Geophysical Research Letters*, *43*(18), 9573–9580. https://doi.org/10.1002/2016GL069820

Yang, X. M., Davis, P. M., & Dieterich, J. H. (1988). Deformation from inflation of a dipping finite prolate spheroid in an elastic half-space as a model for volcanic stressing. *Journal of Geophysical Research*, *93*(B5), 4249–4257. https://doi.org/10.1029/JB093iB05p04249

Yip, S. T. H., Biggs, J., Edmonds, M., Liggins, P., & Shorttle, O. (2022). Contrasting volcanic deformation in arc and ocean island settings due to exsolution of magmatic water. *Geochemistry, Geophysics, Geosystems*, *23*(7), e2022GC010387. https://doi.org/10.1029/2022GC010387